Available online at www.sciencedirect.com

ScienceDirect

Acta Materialia 57 (2009) 2055–2065

Acta MATERIALIA

www.elsevier.com/locate/actamat

Stress and microstructure evolution in thick sputtered films

Andrew J. Detor [a,*], Andrea M. Hodge [b], Eric Chason [c], Yinmin Wang [a], Hongwei Xu [d], Mark Conyers [d], Abbas Nikroo [d], Alex Hamza [a]

[a] Lawrence Livermore National Laboratory, Materials Science and Technology Division, 7000 East Avenue, Livermore, CA 94550, USA
[b] University of Southern California, Department of Aerospace and Mechanical Engineering, Los Angeles, CA, USA
[c] Brown University, Department of Engineering, Providence, RI, USA
[d] General Atomics, 3550 General Atomics Ct., San Diego, CA 92121, USA

Received 11 June 2008; received in revised form 21 December 2008; accepted 28 December 2008
Available online 27 February 2009

Abstract

Materials synthesized by deposition techniques are often plagued by high levels of residual stress. While the origin and control of this stress in thin (sub-micron) films has been an active area of research, it is not clear how the results extrapolate with thickness. In the present work, in situ residual stress measurements are performed during the sputter deposition of beryllium, spanning the transition from thin to thick. Variables including sputtering gas pressure and substrate biasing are shown to strongly affect both the average and instantaneous stress levels measured during film growth. Detailed microstructural characterization is performed to assess the grain structure, surface morphology, and crystallographic growth texture of representative specimens. The microstructure is correlated with theoretical models of stress generation to interpret experimental measurements. A stress map is also constructed, generalizing the effects of processing and material parameters on stress state.

Keywords: Residual stresses; Physical vapor deposition (PVD); Texture; Nanocrystalline microstructure; Thick films

1. Introduction

Thick films are desirable for a variety of applications, ranging from wear and corrosion resistant coatings to free-standing parts. Unfortunately, high levels of residual stress can lead to cracking and/or spalling of the deposited film, posing serious practical problems. In an effort to understand and ultimately control these stresses, a number of studies have been conducted over the past five decades based on experimental [1–15], theoretical [16–29], and computational [30–37] approaches. While earlier studies typically focus on empirical observations of stress and microstructure, more recent investigations are directed at understanding the fundamental, atomic-level mechanisms of stress generation. Tensile stress is most often explained by a grain coalescence mechanism [16–18,21,30,36], where neighboring grains of the growing film are presumed to spontaneously join together under the action of interatomic forces, eliminating two free surfaces in favor of an elastically strained grain boundary. This net in-plane contraction produces tensile stress in the growing film and is expected to be active regardless of the specific synthesis technique or material. Compressive stress models, on the other hand, depend on processing details and generally fall into two categories based on either atomic peening [19,20,28,32] or adatom diffusion [29,37–39]. Atomic peening is likened to the industrial process of shot peening [40], where atoms (or particles) of high incoming energy strike the growing film surface, causing local atomic displacements and densification of the film. Diffusion-based models assume that excess adatoms are incorporated into the grain boundaries during deposition, resulting in densities

---

[*] Corresponding author. Present address: General Electric Global Research, One Research Circle, MB203, Niskayuna, NY 12309, USA. Tel.: +1 518 387 5245.
E-mail address: detor@ge.com (A.J. Detor).

1359-6454/$36.00 © 2009 Acta Materialia Inc. Published by Elsevier Ltd. All rights reserved.
doi:10.1016/j.actamat.2008.12.042

above those expected in equilibrium. Both of these processes are conceptually similar, describing compressive stress as a consequence of densification. However, the routes to densification are fundamentally different, such that diffusion-based models are expected to apply under conditions of high homologous temperature (mobility), while ion peening likely dominates under conditions of high kinetic energy. The overall stress state observed experimentally will involve some competition between the above mechanisms, dependent on the energy supplied to the growing film surface. In the present work, we focus on low temperature magnetron sputtering experiments, paying attention to variables that significantly control the kinetic energy of the deposition process: sputtering gas pressure and substrate biasing.

Sputtering gas pressure has perhaps been the most studied variable to date in terms of residual stress, and there is an almost universally observed transition from tension to compression as pressure is decreased [1,2,5–7,10,11,13,15]. In addition, Thornton and Hoffman [2] observed a clear log-linear trend between the critical tension–compression transition pressure and the atomic mass of the sputtered material; dense, high Z materials exhibit compressive stress to higher sputtering gas pressure as compared to their low Z counterparts. Another well-studied variable in the sputtering process is the effect of substrate biasing, where a negative potential applied to the growing film has been show to induce compressive stress [1,8,14,41–43]. These empirical observations have been broadly rationalized based on the atomic peening mechanism; decreasing sputtering gas pressure or increasing substrate bias both lead to high kinetic energy conditions, tending to yield compressively stressed deposits. Striking a balance between tensile and compressive mechanisms, it should be possible to find a low stress condition for a given experimental setup by simple adjustment of the sputtering gas pressure and/or application of substrate biasing.

In addition to residual stress investigations, research has also been directed at processing–structure relationships in deposited films [1,7,12,44–48]. Common variables, including sputtering gas pressure and substrate biasing, have been correlated with microstructural observations in a variety of materials. One of the earliest and still widely used systems to categorize different structures with respect to processing variables is known as the Thornton zone diagram [44], originally specifying four different "types" of films based loosely on the energy of adatoms. The sequence of types I, T, II, and III corresponds to increasing energy where the microstructure gradually changes from porous columnar grains to fully recrystallized. While this system is instructive for interpreting qualitative trends, it does not incorporate quantitative aspects of the microstructure, such as crystallographic texture or surface roughness, and has not been clearly linked to stress data. In fact, there are relatively few works that combine detailed microstructural characterization with residual stress measurements over a wide range of processing conditions. Also, most of the works cited above have concentrated on thin films, characterized by sub-micron thickness, where researchers examine early-stage film nucleation and growth. Thicker films (>1 μm) have received considerably less attention.

A key question we address in the present work is the connection between thin and thick regimes, and whether thin film stress and microstructure results can be extrapolated to any finite thickness. We explore this connection using an in situ stress measurement technique, enabling real-time information on the evolution of residual stress in films processed over a wide range of sputtering gas pressures and substrate biasing conditions. In addition, we perform detailed microstructural characterization to assess the grain structure, surface morphology, and crystallographic texture during film growth. This combined approach yields a clear picture of the processing–structure–stress relationship beyond the thin film limit. Pure beryllium is used as a model material in the present investigation for a number of reasons. Along with its important role in nuclear fusion energy applications [49–51], beryllium exhibits several unique structural and mechanical properties, making it an interesting test bed for stress–microstructure studies. As a hexagonal metal with the lowest c/a ratio, beryllium shares multiple low surface energy planes [52], which we show to have important consequences on texture selection and film quality. Also, as one of the lightest elements ($Z = 4$), with a high elastic modulus [53], beryllium is especially prone to high levels of tensile stress [2], making it an ideal system to study stress generation and control.

2. Experimental procedures

Beryllium specimens were deposited by magnetron sputtering at General Atomics (San Diego, CA) using three 50.8 mm diameter targets, positioned symmetrically about the center axis of the chamber, operating at 100 W in an argon environment. Silicon $\langle 100 \rangle$ wafers, 25.4 mm in diameter and 525 μm thick, were used as substrates for all experiments, with a substrate-to-target distance of ~90 mm. The substrates were grounded in reference to the chamber wall in all cases, except for the biasing experiments where a -40 V potential was applied. During the biasing experiments only, a $+44$ V potential was also supplied to a 51 mm diameter stainless steel ring located ~6 mm above the substrate to form a secondary plasma near the film surface. This procedure (known as ionized physical vapor deposition) supplies an extra flux of energized ions to the growing film surface; the details of this process are beyond the scope of the present work and the reader is referred to Ref. [54] for more information.

Residual stress measurements were acquired in situ (during film growth) using a multi-beam optical sensor (MOS) system manufactured by k-Space Associates, Inc. (Ann Arbor, MI) [55]. This system uses an array of parallel laser beams reflected from the surface during film growth to measure curvature, which is converted to stress using the Stoney formula [24,27,56]. In all experiments the film/substrate thickness ratio is less than 5×10^{-3}, ensuring the accuracy of this technique [57]. Following deposition, several representative specimens were subject to microstructural characterization using transmission electron microscopy (TEM) for grain size and structure, scanning electron microscopy (SEM) and atomic force microscopy (AFM) for surface morphology, and X-ray diffraction (XRD) for crystallographic texture. A Philips CM300-FEG TEM was used to examine specimens prepared in cross-section by a focused ion beam (FIB) liftout technique [58] in an FEI Nova 600; this DualBeam™ machine was also used for SEM investigations. AFM measurements were performed on a Digital Instruments DIM-300 operating in tapping mode over a scan area of 5 × 5 μm. Traditional θ–2θ (Bragg–Brentano) XRD scans were conducted in reference to the specimen surface on a Philips APD3720 goniometer.

In what follows, we first present the stress results, emphasizing the important information provided by the in situ technique. We then discuss film microstructure, linking the growth morphology to processing conditions and stress data. Finally, the general features observed here are discussed in terms of existing analytical models of stress generation and film growth mechanisms.

3. Stress measurements

In thin film studies, substrate curvature is typically used to provide a measure of the average residual stress. Although the stress may not be uniform, the average value is a useful metric for comparing trends in processing parameters. Average stress is plotted in Fig. 1 for beryllium specimens at three different thicknesses (0.5, 1.0, and 2.0 μm) deposited over a range of sputtering gas pressures without substrate biasing (solid points), and at 5 mTorr with a −40 V bias applied to the substrate (open points). The general trend without biasing is consistent with that observed in the literature for a variety of materials [1,2,5–7,10,11,13,15]; compressive stress at low sputtering gas pressure followed by a tensile peak and slight decline in stress as pressure is increased. In the range of 2–5 mTorr, the sharp transition in stress state is a consequence of the change in energy supplied to the growing film, as mentioned in Section 1 and to be discussed in more detail in Section 5. The slight decline in tensile stress at higher pressures is usually attributed to increasing film porosity under these conditions [1,5,12], such that higher stress levels cannot be supported by the film. Therefore, in cases where dense, high quality films are desired, it is preferable to work in the low pressure range, below ~5 mTorr in the present case. Also demonstrated in Fig. 1 is the significant influence of substrate biasing, where the stress state is reversed from tension to compression at 5 mTorr. This result, again, is generally consistent with that reported in the literature [1,8,14,41–43] and will be discussed from a mechanistic standpoint in Section 5.

While the general trends displayed in Fig. 1 are typical, it is clear that the average stress changes with thickness. This is especially apparent for the lowest 2 mTorr, unbiased and 5 mTorr, biased specimens where stress trends in the tensile direction as film thickness increases. This result has important implications. For example, in studies directed at quantifying the compression–tension transition pressure, critical values would apparently decrease with increasing film thickness. This demonstrates that a single average value does not sufficiently describe the stress state in thick films, where significant gradients in stress are possible. To access the full distribution of stress as a function of thickness, the MOS system provides real-time curvature data, which can be used to calculate the instantaneous stress during film growth. Instantaneous stress is plotted in Fig. 2 for three representative

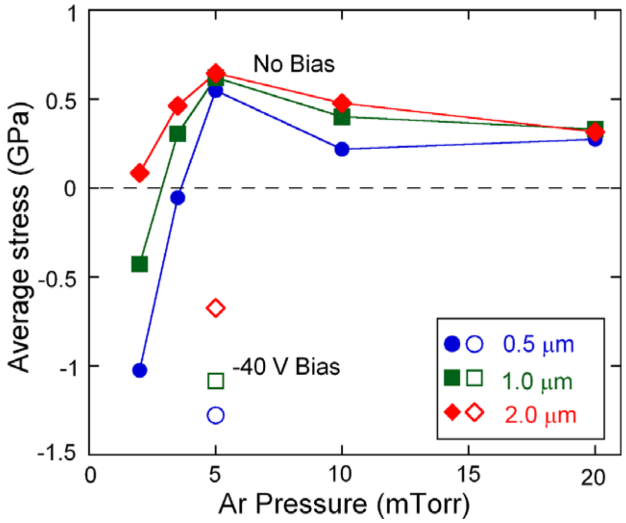

Fig. 1. Average residual stress as a function of sputtering gas pressure for beryllium films of 0.5, 1.0, and 2.0 μm thickness deposited without (closed points) and with (open points) a voltage bias applied to the substrate. Estimated error on the measurement is ±40 MPa based on uncertainties during data acquisition, including variations in temperature and deposition rate. The general trends observed here are consistent with the literature; however, average stress is not constant with thickness for most specimens.

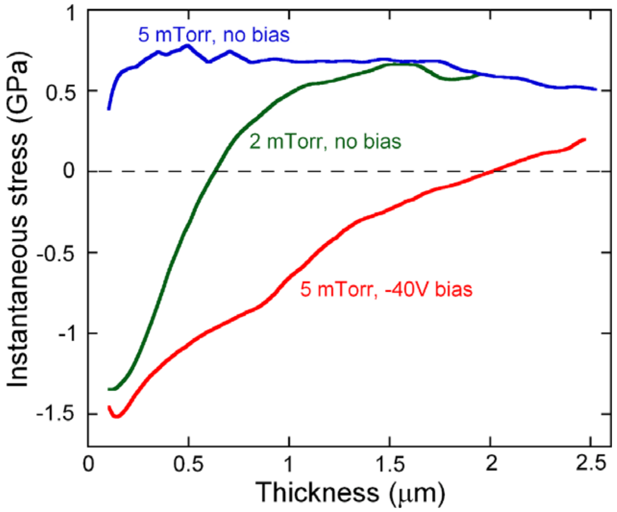

Fig. 2. Instantaneous stress as a function of film thickness for three representative specimens from Fig. 1, encompassing a wide range of stress behavior from tensile to compressive. This instantaneous measure may be directly correlated with the microstructure through-thickness. The error on instantaneous stress is estimated to be ±100 MPa, mainly due to the fitting procedure used to extract the data and temperature/growth rate variations.

specimens from Fig. 1, covering the minimum and maximum stress achieved without substrate biasing (at 2 and 5 mTorr, respectively), and the 5 mTorr, −40 V biased specimen. This instantaneous measure can be interpreted as the increment of stress contributed to the specimen at a particular thickness, at or near the growing surface [4]. While the 5 mTorr, no bias specimen exhibits nearly constant instantaneous stress at ∼500 MPa, both the 2 mTorr, no bias and 5 mTorr, −40 V bias specimens begin in a compressive state and trend in the tensile direction with thickness; these observations are consistent with the average values presented in Fig. 1, which are essentially an integration of the instantaneous data. It is also apparent that the 2 mTorr, no bias specimen reaches a plateau at nearly the same tensile stress level as the 5 mTorr, no bias specimen (∼500 MPa), indicating that there may be an upper bound on achievable tensile stress. This will be discussed in more detail later on. The true attraction of the instantaneous measurement lies in the spatial information; the data in Fig. 2 can be directly compared with the microstructure through-thickness. In the next section, we examine the specimens from Fig. 2 in an effort to interpret the stress trends in relation to microstructural features.

4. Microstructural characterization

Cross-sectional TEM images are presented in Fig. 3a–c for the representative set of processing conditions from Fig. 2, arranged in order of increasing average compressive stress. The full film thickness can be seen in these images with portions of the substrate and surface visible on the left and right, respectively; in Fig. 3a the edge of the FIB liftout specimen can also be seen. Independent of processing conditions, columnar grain growth is clearly observed for all specimens, with an area of dense nucleation near the

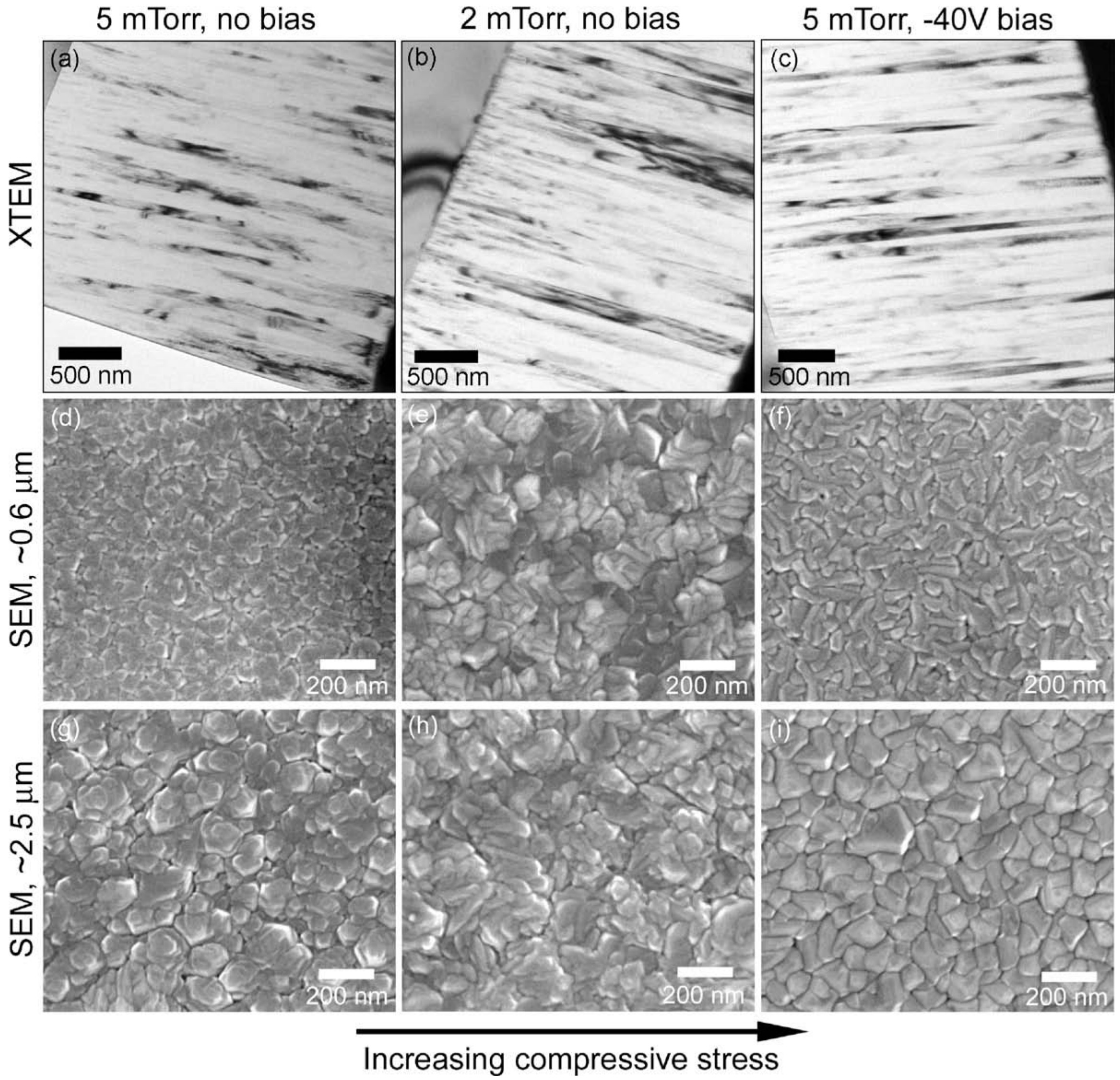

Fig. 3. (a)–(c) Cross-sectional bright-field TEM images of the representative films from Fig. 2, deposited at 5 mTorr with no bias, 2 mTorr with no bias, and 5 mTorr with −40 V substrate bias, respectively. Portions of the substrate (on the left) and film surface (on the right) can be seen in all images. Beneath (a–c) are respective SEM images of the surface morphology for films grown to thicknesses of (d–f) ∼0.6 µm, and (g–i) ∼2.5 µm. Surface structure is strongly influenced by processing conditions.

substrate followed by well-defined grains oriented in the growth direction. In the Thornton classification, these would be designated as zone II structures [44]. Note, however, that a slightly finer grain size is maintained in the biased condition (Fig. 3c) compared with either of the unbiased structures (Fig. 3a and b), with average values near the surface of ~80 and ~130 nm, respectively. Besides this distinction, no clear difference is observed in the grain structure between the three representative specimens.

Surface morphology is examined via SEM in Fig. 3d–i. Images are arranged in columns according to processing condition in the same way as the TEM data, and rows according to thickness: Fig. 3d–f ~0.6 μm and Fig. 3g–i ~2.5 μm. This gives a sense of the change in surface morphology with film growth and the effects of pressure/biasing. For each processing condition, similar features are maintained as thickness increases, with clear coarsening in the case of d → g and f → i. Comparing amongst the representative processing variables reveals significant changes in surface morphology. Nodular (mounding), hexagonal growth patterns are observed for the 5 mTorr, no bias specimen (g) while adding substrate bias at the same pressure leads to a dense, faceted surface structure (i). The 2 mTorr, no bias specimen (h) shares common features between these extremes: areas where faceting is observed and others where the growth appears nodular. These observations suggest a transition in film growth mechanisms between the representative conditions. For a more quantitative understanding of surface morphology, AFM measurements of surface roughness are presented in Fig. 4a and b for each of the specimens from Fig. 3d–i. The AFM data are presented as distributions, showing both the range and relative frequency of surface height observations; root mean square roughness R_q is also listed for each specimen. Several interesting features can be observed here that complement the SEM observations. First, from a thickness of (a) ~0.6 μm to (b) ~2.5 μm the surface structure becomes rougher for all specimens, as indicated by the R_q values, and also by the clear shift and broadening of the peaks. Note that the surface height measurements in (b) are on the order of the grain size observed via TEM mentioned above (~80–130 nm), and that the 5 mTorr, biased specimen maintains the smoothest surface in the thick condition. Second, the 2 mTorr, no bias specimen shows a distinct bimodal distribution in (a), spanning a much wider height range than the other two conditions. The same specimen also displays the broadest distribution in the thick condition (b). In line with the SEM observations, this result suggests that the 2 mTorr, no bias specimen may exhibit multiple growth modes, each with a different characteristic appearance and growth rate.

To examine the growth modes in more detail, XRD measurements are performed on the representative specimens from Fig. 3g–i to quantify crystallographic texture; results are shown in Fig. 5. Strong correlations are

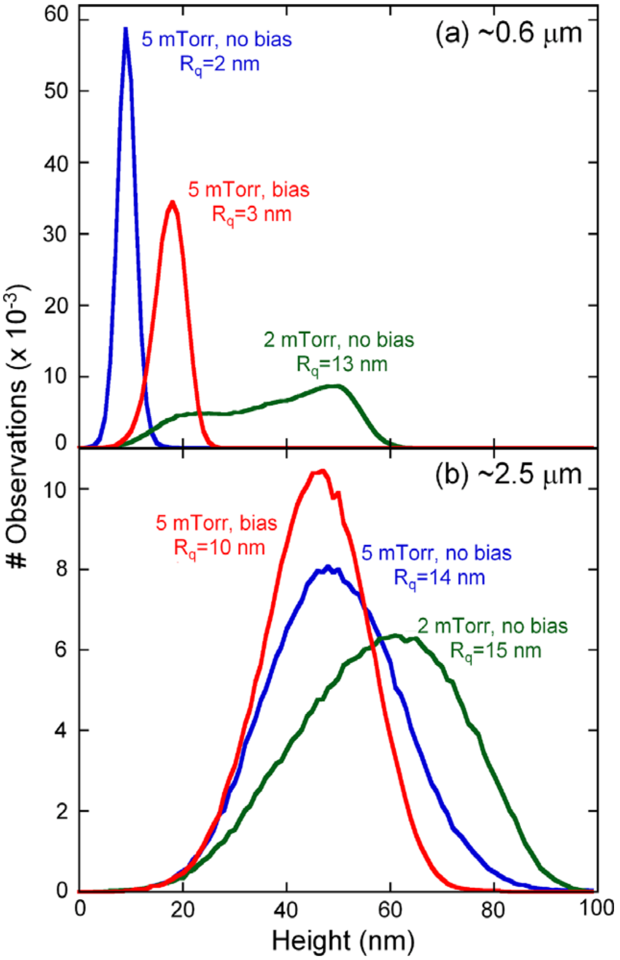

Fig. 4. Surface height distributions extracted from AFM data for the (a) ~0.6 μm thick specimens from Fig. 3d–f and (b) ~2.5 μm thick specimens from Fig. 3g–i. Coarsening is observed in all cases with a unique bimodal distribution for the 2 mTorr, no bias specimen.

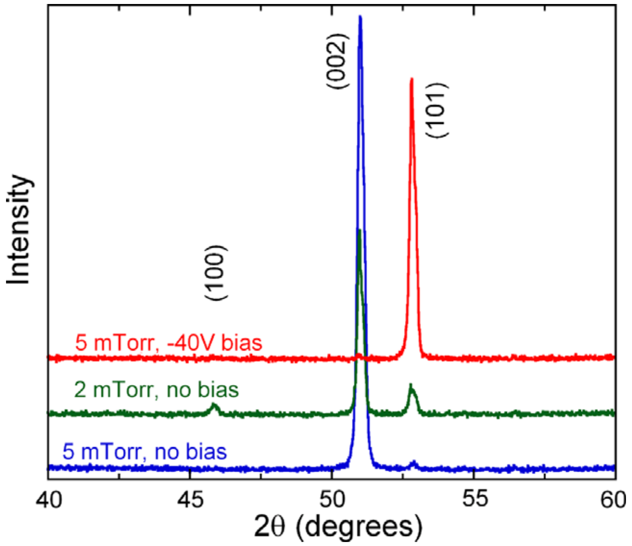

Fig. 5. X-ray diffraction data for the three representative specimens from Fig. 2. A shift in texture is observed from (002) to (101) for the 5 mTorr specimen deposited without and with substrate bias, respectively. The 2 mTorr, no bias specimen shows mixed texture including the (100) prism plane. These results can be used to interpret the growth morphologies observed in Fig. 3d–i, and have important implications for film quality and stress as discussed in the text.

observed between the representative conditions and the (100), (002), and (101) hexagonal planes. While the 5 mTorr, no bias specimen displays nearly perfect (002) basal plane texture, the addition of substrate biasing shifts the dominant texture to the (101) plane. The 2 mTorr, no bias specimen falls between these two extremes, showing both (002) and (101) peaks in addition to a relatively small (100) prism plane signal. Combining the XRD data with the SEM images from Fig. 3 and the AFM measurements from Fig. 4 leads to a clear interpretation of the growth mode for each representative condition. The 5 mTorr, no bias specimen grows with basal texture, leading to the six-fold hexagonal patterning observed in the SEM images (especially apparent for the thick condition, Fig. 3g). A faceted surface morphology is observed with substrate biasing (Fig. 3f and i) because the (101) plane lacks high symmetry. Instead of observing the underlying crystallographic structure, the film grows in such a way to minimize the excess energy from grain boundaries. Intermediate between these two conditions, the 2 mTorr, no bias specimen displays mixed modes of growth.

Based on the above microstructural observations, it is clear that sputtering gas pressure and substrate biasing have significant effects on the growth morphology. In the next section, we interpret these findings in connection with the stress data from Section 3. We also comment on the possible fundamental mechanisms responsible for the observed texture transition, although the details of this are deferred to future work as we are mainly concerned here with the residual stress data.

5. Processing–structure–stress relationship

While a number of theories exist on residual stress generation in deposited films [1,17–20,26,28], it is generally difficult to capture the proposed mechanisms experimentally. This is an area where atomistic [32–34,36] and continuum level [30,31,35] simulations have been successful in providing some understanding beyond the theoretical arguments. In the present work, although the microstructural characterization is performed ex situ, we can directly compare with the in situ stress data to gain some level of understanding from a microstructural point of view. In what follows, we present two models of stress generation based on mechanisms expected to be active in the present experiments, paying special attention to microstructural variables. We then describe a physical model relating processing variables to the stress state based on a critical energy assumption. A map is constructed using this model to help interpret the average stress trends with pressure and substrate biasing observed in the present work, as well as those generally found in the literature. Following this, we discuss the instantaneous stress measurements in Fig. 2 in relation to the microstructural data from Section 4. Finally, we briefly discuss the texture transition revealed by XRD in Fig. 5.

5.1. Tensile stress

One of the first successful models of tensile stress generation was proposed by Doljack and Hoffman [16,17], who considered the stress developed when newly deposited grains are attracted to one another during deposition, causing grain coalescence or “zipping” of the grain boundaries. This in-plane elastic strain produces a biaxial stress in the film. Nix and Clemens [18] later extended this model, using an energetic analysis to derive an upper-bound estimate of residual tensile stress, σ_T, given by:

$$\sigma_T = \left[\frac{Y}{1-v}\cdot\frac{2(2\gamma_s-\gamma_{gb})}{d}\right]^{1/2} \tag{1}$$

where Y is Young’s modulus, v is Poisson’s ratio, d is grain size, and γ_s and γ_{gb} are the surface and grain boundary energies of the film, respectively. This equation is perhaps the most frequently cited to describe tensile stress development in deposited films. Inserting typical values for Be of $Y = 318$ GPa and $v = 0.02$ [59], with assumed surface and grain boundary energies of 1.5 and 0.5 J m^{-2}, respectively, and $d = 100$ nm yields a value of $\sigma_T^{\max} \approx 4$ GPa; significantly higher than that observed experimentally (cf. Figs. 1 and 2). The overestimate of Eq. (1) in comparison to experimental results is well documented in the literature [30], and this continues to be an active area of research. Nevertheless, Eq. (1) provides some insight on the potential atomic level mechanisms involved in tensile stress generation, and a connection to measurable experimental variables. In particular, Eq. (1) suggests that tensile stress should increase with a decrease in grain size and/or an increase in the difference between surface and grain boundary energies. In addition, several more recent studies have extended the simple geometry assumed by Nix and Clemens (flat, hexagonal, columnar grains) [18] to include surface roughness and the effects of grain boundary grooving [25,31,60]. One of the main outcomes of these works is a predicted correlation between roughness and tensile stress; rougher surfaces generate higher tensile stress due to the propensity for in-plane contact between neighboring grain surfaces. Thus, a number of microstructural variables are expected to influence the magnitude of tensile stress generated by the grain coalescence mechanism, and these will be discussed in relation to the present experimental observations in Section 5.4.

5.2. Compressive stress

As mentioned in Section 1, a number of compressive stress models have been presented in the literature, with the most popular involving either atomic peening, or adatom diffusion into grain boundaries, as a means to densify the deposited film. The variables studied in the present experiments (sputtering gas pressure and substrate biasing) mainly affect the kinetic energy of the deposition process and thus ion peening is a natural mechanism to consider as responsible for compressive stress generation [1,19,20,28]. It is important to note, however, that diffusion-based mechanisms may still be active, although we have not included variables here, such as temperature and deposition rate, that enable a systematic study of this effect [29,37–39].

A key requirement of the ion peening mechanism is that the energy of incoming atoms, E, be greater than some critical value, E_{crit}, required to cause local atomic displacements (typically on the order of 10 eV [1,61]). For relatively low fluxes, the models of Windischmann [20] and Davis [19] yield similar results, predicting the level of compressive stress, σ_c, to be:

$$\sigma_C = \kappa \frac{Y}{1-v}\left[\frac{j \cdot E^{1/2}}{R}\right] \tag{2}$$

where R is the total flux of deposited atoms, J is the flux of energetic atoms arriving at the surface (with $E > E_{\text{crit}}$), and κ is a proportionality constant. High energy processing conditions will therefore tend to yield compressively stressed films. Unfortunately, Eq. (2) cannot be applied to estimate stress in the present work because the magnetron sputtering process used does not afford measurement of the j/R ratio or E explicitly. For this reason, other techniques, such as ion beam sputtering [62–65], are more appropriate to study the scaling of Eq. (2) where the researcher has independent control over both energy and flux. However, Eq. (2) does provide insight on the compressive mechanism and, most importantly, it suggest that a critical energy threshold may be used to explain the stress state. If this critical energy is exceeded, the deposit will tend to be compressive.

Several works have studied the underlying physics of the atomic peening mechanism to quantify E_{crit} for various materials [19,20,28,32–34]. As mentioned above, this critical value is typically associated with the atomic displacement energy; an energy barrier that must be overcome to induce atomic rearrangement and compressive stress in the growing film. Values of E_{crit} have been shown to scale roughly as 4–5 times the sublimation energy [61,66], ranging from ~10 to 50 eV for a variety of materials. Furthermore, E_{crit} has been shown to depend on crystallographic orientation [61], with low energy (or close packed) planes typically exhibiting higher threshold values. This orientation dependence may account for as much as ~10 eV deviations. For the specific case of beryllium, ~15 eV is a reasonable estimate for E_{crit} [61,67] and we will use this value as a starting point in our discussion below.

Based on the generalizations introduced above, we may predict the stress state as a function of processing parameters by estimating the energy of incoming atoms/ions on the film surface during deposition. In the next section, we derive an approximate model to link the processing conditions to energy and, in turn, stress.

5.3. Modeling the energetics of sputter deposition

The fundamental process of sputtering has been studied in great detail over the past 50 years. Various aspects of the process including, for example, ion–atom interactions, collision cascades, and sputter yield, have been modeled analytically [67–72] and, more recently, through computer simulation [73–75]. Here, we intend to consolidate some of the most general approximations to quantify the total energy supplied to the surface of a growing film during magnetron sputtering. It must be emphasized that what follows is intended to broadly explain and interpret the present experimental trends, and by no means attempts to capture every detail of the entire sputtering process. For detailed reviews of sputtering theory the reader is referred to Refs. [67,73].

From the perspective of the deposit surface, there are three main possible sources of energy [1]: the sputtered target atoms themselves, t^0, sputtering gas neutrals reflected from the target, g^0, and sputtering gas ions, g^+. Each of these will contribute some amount of energy to the growing film, and here we make the assumption that the total energy, E_{tot}, is additive, such that:

$$E_{\text{tot}} = E_{t^0} + E_{g^0} + E_{g^+} \tag{3}$$

where the subscripts apply to each of the three sources of energy. As an estimate of the sputtered target atom energy, E_{t^0}, we refer to an approximation based on the cohesive energy of the target material, E_{coh} [67]:

$$E_{t^0} \approx \frac{4E_{\text{coh}}}{\alpha} \approx E_{\text{coh}} \cdot \left[\frac{(m_g + m_t)^2}{m_g m_t}\right] \tag{4}$$

where α is the energy transfer mass factor which, in a hard-sphere elastic approximation, depends on the mass of the sputtering gas, m_g, and target, m_t, atoms (α essentially captures the fact that energy transfer is most efficient for collisions between objects (atoms) of similar mass). The relationship in Eq. (4) predicts that the energy of atoms ejected from the surface of a target is directly related to bond strength; i.e. the energy of bonding must be overcome before an atom is ejected from the surface. Indeed, most theoretical works incorporate the cohesive energy in some way [68,73] to describe the energy of sputtered target atoms. Of course the actual energy of sputtered atoms will not be single valued as Eq. (4) suggests, but will instead follow a distribution. In this context, the relationship in Eq. (4) has typically been associated with a threshold (i.e. minimum) energy, where the highest sputter yield also occurs [67,73]. Therefore, Eq. (4) provides a reasonable estimate of the most probable energy of sputtered target atoms, and is particularly useful for making comparisons across different material systems. To further generalize, E_{coh} displays a reasonably linear trend with melting temperature, T_m; a fit to 78 different elements with melting temperatures ranging from −38.9 to 3800 °C yields the relationship $E_{\text{coh}} = 2.06 \times 10^{-3}(T_m) + 1.31$ with an R^2 value of 0.79 [67]. This estimation could be inserted in Eq. (4) to provide an even broader description of sputtered target atom energies using well-known variables. For the case of beryllium, the relationship in Eq. (4) predicts a sputtered target atom energy of ~22 eV, which is in line with that observed for other metals [1], and similar to the estimated value for critical energy ($E_{\text{crit}} \approx 15$ eV) discussed previously.

The second energetic contribution in Eq. (3), E_{g^0}, refers to sputtering gas atoms that have been: (1) accelerated towards the target in ion form, (2) neutralized at the target, and (3) reflected in the direction of the substrate. The energy from these reflected neutrals has been suggested to be the most dominant under conditions of no substrate biasing, tens of electron volts higher than the target atoms discussed above. Windischmann [1] has reviewed this contribution, providing sufficient data to approximate the energy of reflected neutrals as:

$$E_{g^0} \approx 0.1 V_t \left[\frac{m_t}{m_g}\right]^{1/3} \tag{5}$$

where V_t is the voltage applied to the target, assumed here to equal the energy of incoming gas ions accelerated towards the surface (in electron volts). We implicitly neglect the plasma potential here, which in most cases is at least an order of magnitude lower than the target voltage. The mass ratio in Eq. (5) suggests that gas atoms are reflected with higher energy from heavier targets, as has been observed experimentally [72]. For beryllium sputtered in an argon atmosphere with 500 V on the target (typical for the present experiments), Eq. (5) yields a reflected gas atom energy of ~30 eV, slightly higher than that of the target atoms. Note, however, that as beryllium is an extremely light material, this contribution is on the low end compared to more common metals, where reflected neutrals may carry energies approaching 100 eV under the same conditions. This is likely one of the reasons why beryllium is highly prone to tensile stress; the energy contributed to the surface from back-reflected neutrals is relatively low.

The final contribution from charged sputter gas ions, E_{g^+} in Eq. (3), is perhaps the simplest to approximate in the present approach. Identical to our argument for the energy of incoming ions at the target in Eq. (5), we assume that the energy of ions bombarding a biased substrate is equal to the applied voltage:

$$E_{g^+} \approx V_{\text{bias}} \tag{6}$$

A direct relationship of this sort has been suggested in the literature [76,77] and implies that the energy supplied to a growing film surface can be directly tailored through the application of substrate biasing.

At this point we have expressions for each of the three energy terms in Eq. (3). However, before we attempt to correlate the total energy, E_{tot}, with stress data, we must consider the important effects of thermalization, where energetic particles collide with, and lose energy to, residual gas atoms in the chamber. In particular, this will affect the first two terms of Eq. (3) where the neutral target and sputtering gas atoms must travel from the target surface to the substrate. Under biasing conditions the charged gas atoms are accelerated over a relatively short distance above the film surface, and will therefore not be thermalized by scattering to the same degree. To calculate the contribution of this effect, we estimate the number of collisions expected, N, and the energy lost per collision, ϕ, such that the total energy remaining at the film surface is reduced by a factor of $(1-\phi)^N$. The number of collision is simply approximated as the target-to-substrate distance, L, divided by the pressure-dependent mean free path, λ, which is well known in the hard-sphere approximation [67]:

$$N = \frac{L}{\lambda} = L\sqrt{2}\pi x^2 n \approx \frac{Lx^2 P}{9.1 \times 10^{-22}} \tag{7}$$

where x and n are the diameter and density of sputtering gas atoms in the system, respectively, and P is the gas pressure, converted from n assuming the ideal gas law at room temperature. Upon each collision, the energy lost can be approximated as:

$$\phi \approx \frac{(m_t - m_g)^2 + (m_t + m_g)^2}{2(m_t + m_g)^2} \tag{8}$$

again borrowing from the elastic hard-sphere model and assuming an average deflected collision angle of 45° [74]. With these approximations for thermalization, the total energy arriving at the film surface during deposition can be expressed as:

$$E_{\text{tot}} = E_{t^0}(1-\phi)^N + E_{g^0}(1-\phi)^N + E_{g^+} \tag{9}$$

which is simply Eq. (3) with the corrections for energy loss due to scattering.

Inserting Eqs. (4)–(8) into Eq. (9) provides an approximation of the total energy supplied to the film surface, which we will use to define a boundary between tensile and compressive stress under the condition that $E_{\text{tot}} = E_{\text{crit}}$. Eq. (9) is plotted in Fig. 6a with $E_{\text{crit}} = 15$ eV for the case of beryllium sputtered in an argon atmosphere (with $L = 90$ mm and $V_t = 500$ V). This stress map provides a semi-quantitative way of understanding the average stress trends with pressure and biasing observed in the present work and in the literature in general. Under conditions of no substrate biasing the stress transition occurs just below 1 mTorr. At these low pressures the film receives sufficient energy from the target atoms and reflected gas neutrals, such that substrate biasing is not required to activate the compressive mechanism of Eq. (2). At the highest sputtering gas pressures, however, the energy of the target atoms and reflected gas neutral is almost completely thermalized, and the critical energy must be supplied entirely by substrate biasing ($V_{\text{bias}} = E_{\text{crit}}$). Between these extremes both biasing and pressure affect the energy supplied to the film and one can be exchanged for the other (i.e. if substrate bias is decreased, pressure must also be decrease to remain at the critical energy). This interplay between the energy sources defined in Eq. (9) is demonstrated in Fig. 6b, where each term is plotted as a function of sputtering gas pressure under the same conditions as in Fig. 6a. The value for target atoms and reflected neutrals at

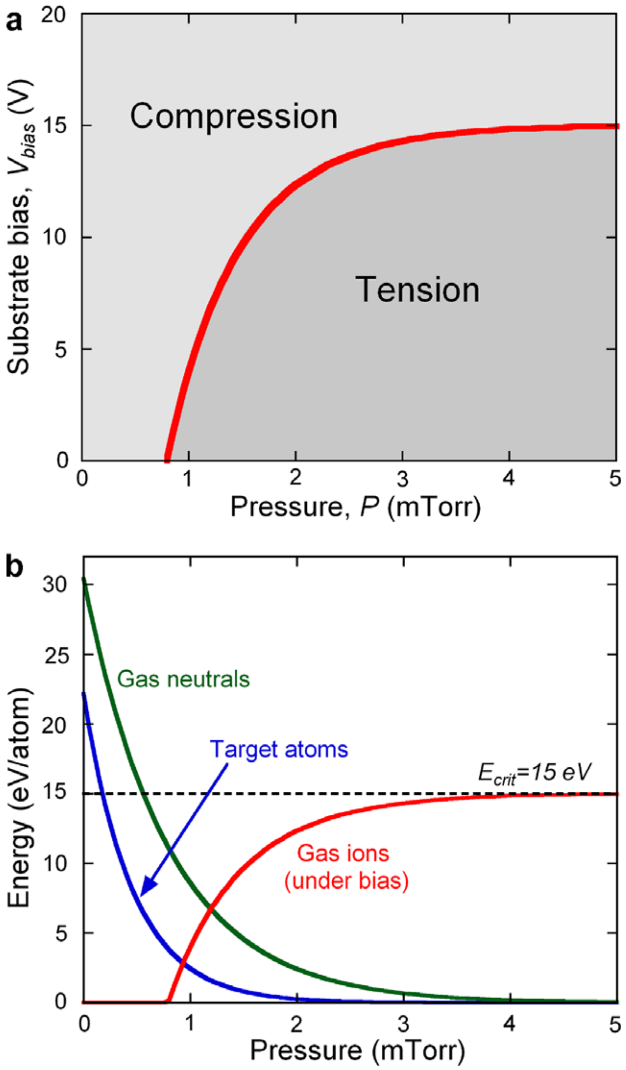

Fig. 6. (a) Stress map constructed by plotting Eq. (9) for the critical condition where energy supplied to the film surface is equal to that required to induce compressive stress ($E_{\mathrm{tot}} = E_{\mathrm{crit}}$). Depositing at low pressure and/or high substrate biasing voltage leads to compressive stress where the ion peening mechanism (cf. Eq. (2)) is activated, and vice versa. (b) Energy contribution from each of the three terms in Eq. (9), showing the effects of thermalization on gas neutrals and target atoms and the increasing importance of substrate biasing required to maintain low stress.

0 mTorr represents the maximum possible energy generated at the target surface, and both sources decrease exponentially with pressure due to thermalization with the sputtering gas. When the total contribution from these two terms is below E_{crit}, substrate biasing must be added to make up the difference.

The construction above provides some general understanding of the average stress trends typically observed with pressure and substrate biasing. In addition, Eq. (9) can be used to evaluate the effects of other parameters, including: target material (through E_{coh} and m_t), sputtering gas type (m_g and x), and substrate-to-target distance (L). Terms appearing in the exponent of Eq. (9) have the most significant effect. For example, changing the substrate-to-target distance from 90 to 10 mm suppresses the tensile region, such that the entire parameter space plotted in Fig. 6a becomes compressive (due to less thermalization). Using Eq. (9) in this way can help interpret and steer experiments toward the desired stress state. Of course, as mentioned throughout the derivation, Eq. (9) relies on a number of simplifying assumptions which may prevent direct, quantitative comparisons. In particular, the results are highly dependent on the assumption of a critical energy (E_{crit}) required to induce compressive stress. Also, there is no incorporation of flux in Eq. (9), which is known to have an important stress contribution (cf. Eq. (4)). Finally, we note that although only the stress state is reported in Fig. 6a, a continuum of stress levels will occur across the boundary, with higher stresses in either direction far from the solution to Eq. (9). In spite of the inherent limitations discussed above, the stress map of Fig. 6a is a useful exercise to help interpret the complex stress results obtained by sputter deposition. Unfortunately, the number of approximations involved in Fig. 6a, and lack of rigorous data in pressure-bias space, prevents direct comparison with experiments. Future work in this area would be useful to verify and expand the present approach.

5.4. Change in stress with film thickness

While the model above is useful for discussing the energetic origins of the average stress trends in Fig. 1, the instantaneous measurements in Fig. 2 require further discussion. In all cases studied, the instantaneous stress ultimately becomes tensile as film thickness increases. Furthermore, an apparent tensile plateau exists at ~500 MPa; instantaneous measurements higher than this have not been observed. This value coincides with the tensile strength of beryllium [59], suggesting a material-dependent upper bound where higher stresses simply cannot be supported by the film. In the absence of cracking, which has not been observed in the present specimens, this implies that some degree of plastic deformation must be occurring during deposition. A second obvious feature in Fig. 2 involves the compressive-to-tensile transition for both the 2 mTorr, no bias, and 5 mTorr, −40 V bias specimens. This trend may be due to a number of factors, which are unfortunately difficult to separate in the present experiments. Variables such as grain size, surface roughness, substrate heating, in-plane crystallographic texture, and impurities are all expected to influence the stress generating mechanisms discussed in Sections 5.1 and 5.2. It is interesting to note that there is no correlation here between stress and grain size as suggested by Eq. (1), which predicts higher tensile stress with finer grain size, as observed in the early stages of growth (cf. Fig. 3a–c). This suggests that other variables may be more important. Viewing the overall stress as a competition among different stress-generating mechanisms, the transition in Fig. 2 may be interpreted as a strengthening and/or weakening of these mechanisms with thickness. For example, as surface roughness increases with film growth, it has been suggested that grain coalescence may become more active [25,31,60], potentially leading to higher tensile stresses. Also, if the developing columnar grains orient to minimize grain boundary energy, this is expected to strengthen the tensile mechanism as the numerator $2\gamma_s - \gamma_{gb}$ becomes larger in Eq. (1). Future studies focused on the in-plane crystallographic orientation would help clarify this potentially important mechanism. It seems reasonable to suspect that a low-energy fiber texture should develop with film growth, making the specimens increasingly prone to tensile stress.

From another perspective, the ion peening or diffusion-based compressive mechanisms may become less effective as the film roughens with growth. Shadowing-induced voids [78] may act as relaxation sites, or the rough surface itself may prevent efficient generation of compressive stress by either mechanism (increasingly oblique ion/atom incidence for the case of ion peening, or longer distances for adatom diffusion). Weakening of the compressive stress generating mechanisms with roughness will shift the balance towards tensile stress in the growing film. This interpretation suggests that maintaining a smooth surface may make it possible to suppress the tensile trend observed with film thickness.

Other contributions from substrate heating and impurities are also possible. However, while slight heating (~70 °C on average) has been recorded in the present experiments, it is not expected to significantly impact mobility given the relatively high melting point of beryllium (1287 °C). Impurities have been proposed as a potential source of compressive stress [1]. Most attention has been paid to lattice distortion or phase changes associated with the incorporation of water vapor, oxygen, hydrogen, and inert sputtering gases. If impurity levels change during film growth, this may lead to non-steady stress conditions. Preliminary RBS measurements found low levels of oxygen and argon impurities in all specimens examined in the present work, with no clear change through thickness within measurement resolution. However, this remains an active area of research and future work will help resolve the impurity contribution in detail.

The instantaneous measurements in Fig. 2 may be interpreted as a combination of the effects discussed above. While the occurrence of a tensile plateau is well justified, future work is needed to understand the origins of the tensile trend with thickness and to generalize this result for other systems.

5.5. Crystallographic texture selection

The texture transition revealed by XRD measurements in Fig. 5 is one of the most important microstructural results. Not only is this transition interesting in terms of fundamental crystal growth mechanisms, but it also has important practical consequences for film quality. From SEM (Fig. 3d–i) and AFM (Fig. 4) measurements the (1 0 1) textured (biased) specimen forms with a smooth, dense surface as compared to growth on the (0 0 2) basal plane. Because of this, thick films may benefit from (1 0 1) texture where roughness and shadowing instabilities are potentially delayed [78]. The underlying physics responsible for this transition and its effects on surface morphology are currently being studied in more detail via additional experiments and atomistic simulations. We note in passing that the (0 0 2), (1 0 1), and (1 0 0) planes all share nearly equal low energy cusps on a Wulff plot for beryllium [52]; thus, slight changes in deposition energetics may be responsible for the massive texture shift observed in the present experiments. More details will be presented on this topic in a future work.

6. Conclusions

The present set of experiments has improved our understanding of residual stress development in thick sputtered films through the use of an in situ measurement technique. While thin films may be adequately characterized by an average stress value, thick films require more detailed measurements where significant gradients in stress are possible through-thickness. For the specific case of magnetron sputtered beryllium, we have found average stress trends consistent with those in the literature for a variety of materials: increasing compressive stress with a decrease in sputtering gas pressure and/or the application of substrate biasing. However, in situ measurements reveal a transition from compressive to tensile stress with film growth. To interpret the stress data, and elucidate processing–structure relationships, detailed microstructural characterization has been performed with the following main conclusions:

- Cross-sectional TEM reveals classic columnar grain growth, with a finer grain size maintained under conditions of substrate biasing.
- Surface morphology is strongly influenced by processing conditions; a transition from rough, hexagonal growth to a smooth, faceted structure is observed with the application of substrate bias.
- A crystallographic texture transition occurs with biasing from (0 0 2) to (1 0 1) preferred growth. This texture transition is reflected in surface morphology observations.

Theoretical models of residual stress generation were examined, including the grain coalescence and atomic peening mechanisms, paying special attention to microstructural variables related to the present experimental findings. Surface roughness, in particular, was correlated with the observed tensile trend during film growth, suggesting that a smooth surface may be required to maintain low levels of stress. A generalized stress map was also developed incorporating simplified expressions for the energetics of deposition, predicting broad relationships between processing/material variables and stress state.

Acknowledgments

This work was performed under the auspices of the US Department of Energy by Lawrence Livermore National Laboratory under Contract DE-AC52-07NA27344.

References

[1] Windischmann H. Crit Rev Solid State Mater Sci 1992;17:547.
[2] Thornton JA, Hoffman DW. Thin Solid Films 1989;171:5.
[3] Hoffman DW. J Vac Sci Technol A 1994;12:953.
[4] Klokholm E, Berry BS. J Electrochem Soc 1968;115:823.
[5] Vink TJ, Somers MAJ, Daams JLC, et al. J Appl Phys 1991;70:4301.
[6] Shen YG, Mai YW, Zhang QC, et al. J Appl Phys 2000;87:177.
[7] Shen YG. Mater Sci Eng A 2003;359:158.
[8] Knoll RW, Bradley ER. Thin Solid Films 1984;117:201.
[9] Hodge AM, Foreman R, Gallegos GF. J Nucl Mater 2005;342:8.
[10] Tranchant J, Angleraud B, Tessier PY, et al. Surf Coat Technol 2006;200:6549.
[11] Andritschky M, Teixeira V. Vacuum 1992;43:455.
[12] Misra A, Nastasi M. J Mater Res 1999;14:4466.
[13] Cuthrell RE, Mattox DM, Peeples CR, et al. J Vac Sci Technol A 1988;6:2914.
[14] Catania P, Roy RA, Cuomo JJ. J Appl Phys 1993;74:1008.
[15] Yoshihara T, Suzuki K. J Vac Sci Technol B 1993;11:301.
[16] Doljack FA, Hoffman RW. Thin Solid Films 1972;12:71.
[17] Hoffman RW. Thin Solid Films 1976;34:185.
[18] Nix WD, Clemens BM. J Mater Res 1999;14:3467.
[19] Davis CA. Thin Solid Films 1993;226:30.
[20] Windischmann H. J Appl Phys 1987;62:1800.
[21] Freund LB, Chason E. J Appl Phys 2001;89:4866.
[22] Sheldon BW, Bhandari A, Bower AF, et al. Acta Mater 2007;55:4973.
[23] Knuyt G. Thin Solid Films 2004;467:275.
[24] Sheldon BW, Rajamani A, Bhandari A, et al. J Appl Phys 2005;98:043509.
[25] Sheldon BW, Lau KHA, Rajamani A. J Appl Phys 2001;90:5097.
[26] Tello JS, Bower AF, Chason E, et al. Phys Rev Lett 2007;98:216104.
[27] Floro JA, Chason E, Cammarata RC, et al. MRS Bull 2002;27:19.
[28] Carter G. J Phys D 1994;27:1046.
[29] Guduru PR, Chason E, Freund LB. J Mech Phys Solids 2003;51:2127.
[30] Seel SC, Thompson CV, Hearne SJ, et al. J Appl Phys 2000;88:7079.
[31] Seel SC, Thompson CV. J Appl Phys 2003;93:9038.
[32] Marks NA, McKenzie DR, Pailthorpe BA. Phys Rev B 1996;53:4117.
[33] Bilek MMM, McKenzie DR. Surf Coat Technol 2006;200:4345.
[34] Koster M, Urbassek HM. Phys Rev B 2001;63:224111.
[35] Rajamani A, Sheldon BW, Chason E, et al. Appl Phys Lett 2002;81:1204.
[36] Seel SC, Hoyt JJ, Webb EB, et al. Phys Rev B 2006;73:245402.
[37] Buehler MJ, Hartmaier A, Gao HJ. J Mech Phys Solids 2003;51:2105.
[38] Chason E, Sheldon BW, Freund LB, et al. Phys Rev Lett 2002;88.
[39] Pao CW, Foiles SM, Webb EB, et al. Phys Rev Lett 2007;99.
[40] Kobayashi M, Matsui T, Murakami Y. Int J Fatigue 1998;20:351.
[41] Janssen GCAM, Kamminga JD. Appl Phys Lett 2004;85:3086.
[42] Ljungcrantz H, Hultman L, Sundgren JE, et al. J Appl Phys 1995;78:832.
[43] Kim SP, Choi HM, Choi SK. Thin Solid Films 1998;322:298.
[44] Thornton JA. Annu Rev Mater Sci 1977;7:239.
[45] Thornton JA. J Vac Sci Technol 1974;11:666.
[46] Thornton JA. J Vac Sci Technol 1975;12:830.
[47] Messier R, Giri AP, Roy RA. J Vac Sci Technol A 1984;2:500.
[48] Petrov I, Barna PB, Hultman L, et al. J Vac Sci Technol A 2003;21:S117.
[49] Billone MC, Dalledonne M, Macaulay-Newcombe RG. Fusion Eng Des 1995;27:179.
[50] Dittrich TR, Haan SW, Marinak MM, et al. Phys Plasmas 1999;6:2164.
[51] Haan SW, Amendt PA, Dittrich TR, et al. Nucl Fusion 2004;44:S171.
[52] Matysina ZA. Mater Chem Phys 1999;60:70.
[53] Migliori A, Ledbetter H, Thoma DJ, et al. J Appl Phys 2004;95:2436.
[54] Helmersson U, Lattemann M, Bohlmark J, et al. Thin Solid Films 2006;513:1.
[55] kSA Multi-beam optical sensor (MOS) system, k-Space Associates, Inc. Available from: http://www.k-space.com.
[56] Stoney GG. Proc Roy Soc Lond A 1909;82:172.
[57] Freund LB, Floro JA, Chason E. Appl Phys Lett 1999;74:1987.
[58] Mayer J, Giannuzzi LA, Kamino T, et al. MRS Bull 2007;32:400.
[59] Gale WF, Totemeier TC, editors. Smithells metals reference book. Boston (MA): Elsevier/Butterworth–Heinemann; 2004.
[60] Carroll MS, Verley JC, Sheng JJ, et al. J Appl Phys 2007;101:063540.
[61] Kenik EA, Mitchell TE. Philos Mag 1975;32:815.
[62] Debelle A, Abadias G, Michel A, et al. J Vac Sci Technol A 2007;25:1438.
[63] Bilek MMM, Verdon M, Ryves L, et al. Thin Solid Films 2005;482:69.
[64] Ino K, Shinohara T, Ushiki T, et al. J Vac Sci Technol A 1997;15:2627.
[65] Mirkarimi PB, Mccarty KF, Medlin DL, et al. J Mater Res 1994;9:2925.
[66] Seitz F. Discus Faraday Soc 1949;5:271.
[67] Mahan J. Physical vapor deposition of thin films. New York (NY): Wiley; 2000.
[68] Sigmund P. Phys Rev 1969;184:383.
[69] Oechsner H. Appl Phys 1975;8:185.
[70] Westwood W. Prog Surf Sci 1976;7:71.
[71] Stuart RV, Wehner GK, Anderson GS. J Appl Phys 1969;40:803.
[72] Gesang WR, Oechsner H, Schoof H. Nuc Inst Methods 1976;132:687.
[73] Gnaser H. Energy and angular distributions of sputtered species. In: Behrisch R, Eckstein E, editor. Sputtering by particle bombardment, vol. 110. Berlin: Springer; 2007. p. 231.
[74] Motohiro T, Taga Y. Thin Solid Films 1984;112:161.
[75] Vargheese KD, Rao GM. J Appl Phys 2000;87:7544.
[76] Sarakinos K, Alami J, Karimi PM, et al. J Phys D 2007;40:778.
[77] Bergman C. Surf Coat Technol 1988;36:243.
[78] Mahieu S, Ghekiere P, Depla D, et al. Thin Solid Films 2006;515:1229.